Atmos. Chem. Phys., 16, 8071–8080, 2016
www.atmos-chem-phys.net/16/8071/2016/
doi:10.5194/acp-16-8071-2016

Atmospheric Chemistry and Physics Open Access EGU

Global fine-mode aerosol radiative effect, as constrained by comprehensive observations

Chul E. Chung[1], Jung-Eun Chu[2], Yunha Lee[3], Twan van Noije[4], Hwayoung Jeoung[5], Kyung-Ja Ha[2], and Marguerite Marks[6]

[1]Division of Atmospheric Science, Desert Research Institute, Reno, NV 89512, USA
[2]Dept. Atmospheric Sciences, Pusan National University, Busan 46241, South Korea
[3]Washington State University, Pullman, WA 99164, USA
[4]Royal Netherlands Meteorological Institute, 3730 AE De Bilt, the Netherlands
[5]National Meteorological Satellite Center, 27803, South Korea
[6]Dept. Civil and Environmental Engineering, Carnegie Mellon University, Pittsburgh, PA 15213, USA

Correspondence to: Chul E. Chung (eddy.chung@dri.edu)

Received: 13 January 2016 – Published in Atmos. Chem. Phys. Discuss.: 22 January 2016
Revised: 20 May 2016 – Accepted: 13 June 2016 – Published: 4 July 2016

Abstract. Aerosols directly affect the radiative balance of the Earth through the absorption and scattering of solar radiation. Although the contributions of absorption (heating) and scattering (cooling) of sunlight have proved difficult to quantify, the consensus is that anthropogenic aerosols cool the climate, partially offsetting the warming by rising greenhouse gas concentrations. Recent estimates of global direct anthropogenic aerosol radiative forcing (i.e., global radiative forcing due to aerosol–radiation interactions) are $-0.35 \pm 0.5\,\mathrm{W\,m^{-2}}$, and these estimates depend heavily on aerosol simulation. Here, we integrate a comprehensive suite of satellite and ground-based observations to constrain total aerosol optical depth (AOD), its fine-mode fraction, the vertical distribution of aerosols and clouds, and the collocation of clouds and overlying aerosols. We find that the direct fine-mode aerosol radiative effect is $-0.46\,\mathrm{W\,m^{-2}}$ (-0.54 to $-0.39\,\mathrm{W\,m^{-2}}$). Fine-mode aerosols include sea salt and dust aerosols, and we find that these natural aerosols result in a very large cooling (-0.44 to $-0.26\,\mathrm{W\,m^{-2}}$) when constrained by observations. When the contribution of these natural aerosols is subtracted from the fine-mode radiative effect, the net becomes -0.11 (-0.28 to $+0.05$) $\mathrm{W\,m^{-2}}$. This net arises from total (natural + anthropogenic) carbonaceous, sulfate and nitrate aerosols, which suggests that global direct anthropogenic aerosol radiative forcing is less negative than $-0.35\,\mathrm{W\,m^{-2}}$.

1 Introduction

Atmospheric aerosols absorb and scatter solar radiation and act as cloud condensation nuclei, thus affecting cloud albedo and lifetime. The climatic effect of anthropogenic aerosols is usually quantified in terms of radiative forcing, defined as the net radiative flux perturbation at the top of the atmosphere (TOA) owing to aerosol changes from preindustrial times to the present. The magnitude of aerosol radiative forcing is recognized as the most uncertain component of estimated total radiative forcing (Myhre et al., 2013a). The magnitude of the global average of aerosol direct radiative forcing (which is referred to as radiative forcing due to aerosol–radiation interactions in the 5th IPCC report) has been estimated to range from -0.85 to $+0.15\,\mathrm{W\,m^{-2}}$ (Myhre et al., 2013a).

Direct aerosol forcing has been commonly estimated by a model-based approach of simulating global aerosol amount, distribution and characteristics and by processing the predicted global aerosol distribution by a radiation model. Global aerosol simulations are subject to large uncertainties in emissions, transport, gas-to-aerosol conversion, aerosol aging, aerosol mixing state, and wet and dry deposition (Bond et al., 2004; Ma et al., 2012). The large spread among direct aerosol forcing estimates (Myhre et al., 2013a) is attributable largely to these simulation uncertainties. Furthermore, processing the calculated aerosol distribution by a radiation model requires the specification of parameters such as

the single scattering albedo (SSA) of organic aerosol, which has been considered to be 0.96 to 1.0 at 550 nm in the modeling community (Myhre et al., 2013b) but may actually be much lower (e.g., 0.85 estimated by Magi, 2009, 2011). Attempts have been made to bypass some of these uncertainties and constrain calculated aerosol optical properties by observations (Chung et al., 2005; Bellouin et al., 2008; Myhre, 2009; Su et al., 2013), but these semiempirical studies are not sufficient to validate the model-based estimates given heavy model dependence. In particular, the anthropogenic fraction of the aerosol amount was obtained entirely from aerosol simulations (Chung et al., 2005; Myhre, 2009; Su et al., 2013) or by utilizing the fine-mode fraction (FMF) of satellite-derived AOD (aerosol optical depth) over ocean (Bellouin et al., 2008; Chung et al., 2005). Over the land, where most anthropogenic aerosols are located, no study has constrained the anthropogenic fraction by observations yet.

Aerosols have different sizes and typically follow a bimodal structure in terms of fine mode and coarse mode (Kim et al., 2007; Viskari et al., 2012). Fine-mode aerosols usually have submicron diameter sizes and these small particles are mostly anthropogenic. In this study, we provide observational estimates of the direct fine-mode aerosol radiative effect (i.e., anthropogenic + natural forcing due to all the fine-mode aerosols). In particular, we constrain total AOD, SSA and the asymmetry parameter by observations as in previous semiempirical studies (Chung et al., 2005; Myhre, 2009; Su et al., 2013). In addition, we use observations to constrain the aerosol vertical profile and the FMF of AOD over land as well as ocean. There is some use of simulated aerosol to fill in observation gaps in our study, but the use is highly limited, and we address the uncertainty due to the use of simulation. When our observational estimates are compared to the simulated fine-mode aerosol radiative effects, one can obtain additional insights into biases and uncertainties in the aerosol forcing estimates from aerosol simulations.

Atmospheric aerosols consist of carbonaceous, sulfate, nitrate, sea salt and dust aerosols. The first three types of aerosols are fine-mode particles, which are mostly anthropogenic, while a sizable portion of sea salt and dust aerosols are also in the fine mode. Thus, offering observational estimates of fine-mode aerosol radiative effect is an important advance but is not sufficient in understanding the biases in the aerosol forcing estimates from aerosol simulations. In the present study, we will use observations to constrain the fine-mode sea salt and dust AODs as well and offer estimates of aerosol radiative effect due to fine-mode sea salt and dust aerosols.

2 Data

In Sect. 4 and Table 1, aerosol direct radiative effects (DRE) will be computed for three cases: (i) for total aerosols, (ii) for the fine mode (including natural fine-mode particles), and (iii) for fine-mode sea salt and dust. The total and fine-mode AOD are based on observations, as explained in Sect. 2.1. The other aerosol optical properties needed for the DRE calculations are derived as follows:

- The asymmetry parameter (ASY), SSA and the coalbedo Ångström exponent (CAl_AE) for the total aerosols are derived by nudging GOCART simulated values towards AERONET data (Sect. 2.2). The spectral dependence of ASY is addressed as in Chung et al. (2005).

- The fine-mode aerosol DRE is computed as the difference between the total and coarse-mode DREs. The coarse-mode ASY, SSA and CAl_AE are derived from GOCART simulations, as explained in Sect. 2.3.

- For computing the DRE due to fine-mode sea salt and dust, ASY, SSA and CAl AE are derived from GOCART simulations (Sect. 2.3).

The datasets used to derive this information are explained in the following. All the datasets used in this study are monthly means.

2.1 Global observational data

AOD is a common measure of aerosol amount. AERONET (Aerosol Robotic Network; Holben et al., 1998) AOD is known to be the most accurate global-scale product. However, AERONET sites are non-uniformly distributed over the globe, while less reliable satellite (MODIS and MISR) AODs have nearly full global coverage. We follow the approach of Chung et al. (2005) and Lee and Chung (2013) in nudging or adjusting the satellite AOD towards AERONET AOD to construct globally reliable AOD from 2001 to 2010. See Chung et al. (2005) and Lee and Chung (2013) for the visual effects of the nudging. Figure 1a shows this adjusted AOD. Also, the AOD Ångström exponent from 2001 to 2010 is derived by adjusting the satellite data towards AERONET data as in Lee and Chung (2013).

Fine-mode AOD (fAOD) at 500 nm from 2001 to 2010 are obtained by the approach in Lee and Chung (2013), except that instead of directly using the monthly AERONET FMF data we used the monthly AERONET fAOD (from the direct sun measurements and the spectral deconvolution algorithm as in Lee and Chung) and total AOD to derive the FMF. Like in Lee and Chung (2013), we convert AOD Ångström exponent data into FMF data and nudge this FMF data towards AERONET FMF data to derive reliable FMF and thus fine-mode AOD over the globe. Note that the definition of fine mode in the present study thus follows that by the AERONET spectral deconvolution algorithm as in O'Neill et al. (2003) and Lee and Chung (2013). Coarse-mode AOD at 500 nm is obtained by subtracting fine-mode AOD from total AOD at 500 nm.

Table 1. Global 2001–2010 average of aerosol radiative effect calculated with the Monte-Carlo Aerosol Cloud Radiation (MACR) model. In this table, natural aerosol radiative effects are included. All the aerosol radiative effect estimates made by the MACR model in this study include 3-D cloud effects.

Direct aerosol radiative effect	Run	TOA (in W m^{-2})	Atmosphere	Surface
(Total) direct aerosol radiative effect		−2.28	+4.77	−7.05
Fine-mode radiative effect	baseline	−0.46	+3.88	−4.33
Fine-mode radiative effect	sensitivity run 1: least absorbing case	−0.54	+3.63	−4.17
Fine-mode radiative effect	sensitivity run 2: most absorbing case	−0.39	+4.08	−4.47
Fine-mode sea salt and dust radiative effect	baseline: ModelE2 with reduced dust FMF	−0.35	+0.23	−0.58
Fine-mode sea salt and dust radiative effect	sensitivity run 1: reduced GOCART dust FMF + ModelE2 sea salt FMF	−0.26	+0.16	−0.42
Fine-mode sea salt and dust radiative effect	sensitivity run 2: reduced ModelE2 dust FMF, + ModelE2/GOCART/TM5 mixed sea salt FMF	−0.44	+0.26	−0.70
Fine-mode radiative effect without dust and sea salt	baseline	−0.11	+3.64	−3.75

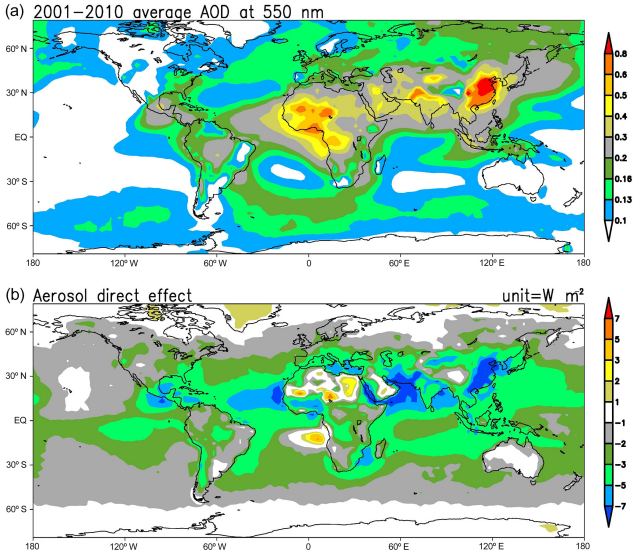

Figure 1. (a) The 2001–2010 mean 550 nm AOD obtained by integrating MODIS, MISR and AERONET AOD. **(b)** The 2001–2010 mean direct aerosol radiative effect at TOA, as estimated by a radiation model that includes observationally derived surface albedo. The aerosol radiative effect estimate here includes natural aerosols.

We computed the 2001–2010 average for each calendar month at the T42 resolution. In these datasets, the observational data gaps are filled by the GOCART simulation (Chin et al., 2002) as in Lee and Chung (2013). These data gaps are predominantly confined to the polar regions and are even fewer in polar summer.

We obtain fAOD at 550 nm by subtracting coarse-mode AOD at 500 nm from AOD at 550 nm, assuming that coarse-mode AOD does not change from 500 to 550 nm. That is, $\mathrm{fAOD}_{550} = \mathrm{fAOD}_{500} + (\mathrm{AOD}_{550} - \mathrm{AOD}_{500})$. Total AOD at any wavelength is obtained by combining AOD at 550 nm and the AOD Ångström exponent.

2.2 Global semi-observational data

To compute the direct aerosol radiative effect, aerosol optical characteristics, such as SSA, must be specified. We construct a global distribution of SSA by nudging global model-simulated (Chin et al., 2002) SSA towards AERONET SSA. We apply a similar procedure to ASY.

550 nm SSA, 550 nm ASY and CAl_AE (co-albedo Ångström exponent; Co-albedo = 1-SSA) for total (natural + anthropogenic) aerosols are obtained by nudging the GOCART simulation (Chin et al., 2002) towards AERONET data. Specifically, for ASY and CAl_AE the following nudging equation is used:

$$\mathrm{N\_ASY}_j = \mathrm{G_{ASY}}_j + \frac{\sum_i \frac{\mathrm{AERONET\_ASY}_i - \mathrm{G\_ASY}_i}{d_{j,i}^4}}{\sum_i \frac{1}{d_{j,i}^4}}, \quad (1)$$

where $\mathrm{N\_ASY}_j$ is the adjusted new value of ASY at grid j; $\mathrm{AERONET\_ASY}_i$ is an AERONET ASY at station i; $d_{j,i}$ is the distance between j and i; and $\mathrm{G\_ASY}_i$ is the GOCART ASY at the grid box containing $\mathrm{AERONET}_i$. Here the AERONET data and the GOCART simulation are on the T42 grids.

For SSA, the following equation is used:

$$(1 - \mathrm{N\_SSA}_j) = (1 - \mathrm{G\_SSA}_j) \times \frac{\sum_i \frac{1 - \mathrm{AERONET\_SSA}_i}{d_{j,i}^4}}{\sum_i \frac{1 - \mathrm{G\_SSA}_i}{d_{j,i}^4}}. \quad (2)$$

Another way to interpret the above equations (Eqs. 1, 2) is that the GOCART simulation is an interpolation tool. The

equation for SSA differs from that for ASY or CAL_AE, because SSA cannot be negative, and its value goes down from 1.0. The above equations are applied for each grid and each calendar month. The final values are the simulation nudged towards AERONET values. Please note that these above equations (Eqs. 1 and 2) were also used in Chung et al. (2005), but a clear explanation was not given in that study.

Before combining the GOCART simulation and AERONET data, the 2001–2010 average was calculated from the monthly Level 2.0 AERONET data for each calendar month. The average of the AERONET SSA or ASY was AOD-weighted. Then, SSA and ASY at 550 nm were obtained from the neighboring wavelength values through linear interpolation. AERONET CAl_AE was obtained by the 2001–2010 SSA averages at 440, 675 and 870 nm for each calendar month. Please note that AERONET only gives Level 2.0 quality SSA when AOD at 440 nm > 0.4, and therefore many regions of the Earth do not have AERONET SSA data.

The products from combining the GOCART simulation and AERONET data are semi-observational, and we address the model dependence as follows.

SSA, apart from AOD, is the most influential parameter in aerosol direct forcing (Chung, 2012). We first generated three different sets of simulated SSA:

$$\begin{aligned}\text{SSA1} = (&0.19 \times \text{BC\_AOD} + 0.85 \times \text{OA\_AOD} + 1.0 \\ &\times \text{sulfate\_AOD} + 1.0 \times \text{sea-salt\_AOD} + 0.96 \\ &\times \text{dust\_AOD})/\text{total\_AOD};\end{aligned}$$

$$\begin{aligned}\text{SSA2} = (&0.14 \times \text{BC\_AOD} + 0.8 \times \text{OA\_AOD} + 1.0 \\ &\times \text{sulfate\_AOD} + 1.0 \times \text{sea-salt\_AOD} + 0.96 \\ &\times \text{dust\_AOD})/\text{total\_AOD};\ \text{and}\end{aligned}$$

$$\begin{aligned}\text{SSA3} = (&0.19 \times \text{BC\_AOD} + 0.98 \times \text{OA\_AOD} + 1.0 \\ &\times \text{sulfate\_AOD} + 1.0 \times \text{sea-salt\_AOD} + 0.96 \\ &\times \text{dust\_AOD})/\text{total\_AOD}.\end{aligned}$$

BC_AOD above refers to the GOCART BC AOD at 550 nm. We chose parameters (e.g., 0.19 for BC SSA) in the above three SSA equations from various observational studies (e.g., Magi, 2009, 2011). Additionally, in SSA2 (more absorbing case), we doubled the magnitude of BC AOD, given a suggestion (e.g., Chung et al., 2012) that simulated BC is significantly underestimated. We use the above three sets of simulated SSA in order to produce an initial estimate of the uncertainty in simulated SSA. Then, we nudged the three sets of simulated SSA towards the same AERONET SSA, which gave three sets of semi-observational SSA. Finally, we computed the average, maximum and minimum SSAs from the three sets of SSA over each grid and each calendar month, and then we regenerated three sets of SSA (average (baseline), maximum; and minimum; see Fig. 2). This regeneration increases the global-average SSA difference between the least absorbing and most absorbing cases. We do this regeneration in an attempt to fully bracket the simulated SSA uncertainty. The last procedure (i.e., regeneration) ensures that the final three sets of SSA depend insignificantly on the initial estimate of the simulated SSA uncertainty.

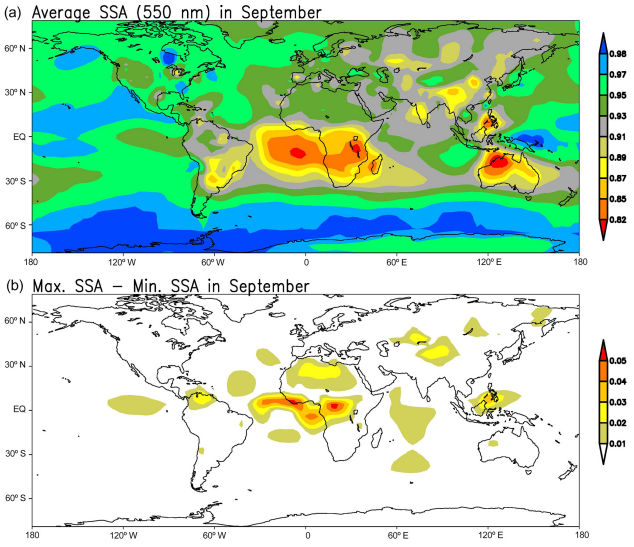

Figure 2. Integration of simulated SSA and AERONET SSA. **(a)** Average SSA. **(b)** Maximum SSA – minimum SSA.

Simulated ASY at 550 nm and CAl_AE are computed as follows.

$$\begin{aligned}\text{ASY} = (&0.6 \times \text{CA\_SAOD} + 0.7 \times \text{sulfate\_SAOD} + 0.75 \\ &\times \text{sea-salt\_SAOD} + 0.75 \times \text{dust\_SAOD})/\text{total\_SAOD}.\end{aligned}$$

CA_SAOD here refers to carbonaceous aerosol (i.e., BC + OA) SAOD (scattering AOD) at 550 nm from GOCART.

$$\begin{aligned}\text{CAl\_AE} = (&-0.53 \times \text{CA\_AOD} + 2.215 \\ &\times \text{dust\_AOD})/\text{total\_AOD},\end{aligned}$$

where CA_AOD refers to CA AOD. The chosen parameters (e.g., 2.215) in the ASY and CAl_AE equations are from preliminary AERONET data analysis. These simulated ASY and CAl_AE were nudged towards AERONET data as explained earlier. We do not address the model dependence on ASY or CAl_AE, since its impact on aerosol forcing is tiny compared to the impact of SSA uncertainty. To be certain, we regenerated the ASY using doubled BC AOD while holding other components (such as SSA) fixed and found that the global direct aerosol effect changes by less than 0.002 W m^{-2}.

The GOCART simulations were prepared as follows. We used sea salt AOD from Chin et al. (2002) and BC (black carbon), OA (organic aerosol), dust and sulfate AODs from the Giovanni website (http://gdata1.sci.gsfc.nasa.gov/daac-bin/G3/gui.cgi?instance_id=neespi), which contains GOCART model output from 2000 to 2007. These AODs are monthly means at 550 nm. Then, the climatological seasonal cycle for

the available data period was computed. We used these simulated AOD values to compute the simulated SSA, ASY and CAL_AE.

2.3 Global simulations

For coarse-mode aerosols, we assumed ASY to be 0.75 and the AOD Ångström exponent to be 0.0. For 550 nm SSA and CAL_AE, we rely entirely on the GOCART simulations as follows: $\mathrm{SSA} = (1.0 \times \text{sea-salt\_AOD} + 0.96 \times \text{dust\_AOD})/\text{lAOD}$, where dust_AOD refers to GOCART dust AOD and lAOD refers to GOCART dust and sea salt AODs combined; $\mathrm{CAL\_AE} = 2.215 \times \text{dust\_AOD}/\text{lAOD}$. Although we rely entirely on simulated SSA for coarse-mode aerosols, we find a very small coarse-mode aerosol radiative effect uncertainty resulting from simulated SSA. For instance, when we change the dust AOD by 35 %, the difference in coarse-mode aerosol radiative effect is only 0.01 W m^{-2}.

For fine-mode sea salt and dust aerosols, we assumed ASY to be 0.6 and the AOD Ångström exponent to be 1.85. For 550 nm SSA and CAL_AE, we rely entirely on simulated fAODs as follows:

$$\mathrm{SSA} = (1.0 \times \text{sea-salt\_fAOD} + 0.96 \times \text{dust\_fAOD})/\text{fAOD},$$

where dust_fAOD refers to dust fAOD and fAOD refers to dust and sea salt fAODs combined; $\mathrm{CAL\_AE} = 2.215 \times \text{dust\_fAOD}/\text{lAOD}$.

These simulated aerosol optical properties were used in the Monte-Carlo Aerosol Cloud Radiation (MACR) model runs, leading to the results in Table 1.

2.4 Vertical profile

Aerosol vertical profiles are obtained from the space-borne CALIOP lidar (Liu et al., 2009). To construct the profile, we used the daytime CALIPSO lidar Level 2.0 data (Liu et al., 2009) from June 2006 to October 2011. We processed the Level 2.0 data and obtained a clear-sky aerosol extinction coefficient at 532 nm at the T42 spatial resolution and 500 m MACR model vertical resolution. We filled the data gaps using available neighboring data through linear interpolation. We then computed the climatological seasonal cycle for the entire available data period. Over some grids and calendar months, the aerosol extinction coefficient has extremely low magnitudes, in which case, the planetary boundary layer (PBL) profile as in Chung et al. (2012) is applied. The threshold for applying the PBL profile is a vertically summed aerosol extinction coefficient of 0.03. Note that a vertically summed aerosol extinction coefficient of 0.03 is associated with a very small amount of aerosol and the effect of these aerosols on the global aerosol direct effect is very small. Also note that the aerosol vertical profile from CALIPSO is scaled to match the AOD observations obtained by integrating AERONET, MODIS and MISR data (as shown in Fig. 1a) since the latter observations describe clear-sky AOD too and give better accuracy. The clear-sky aerosol profile from CALIPSO is assumed to be applied to an entire T42 grid in the MACR model.

To adjust the magnitude of AOD over cloud by CALIPSO data, we use the daytime CALIPSO lidar Level 3.0 data (Winker et al., 2013), which are globally gridded ($5^\circ \times 2^\circ$) monthly mean data spanning June 2006 to January 2012. Specifically, we use the CALIPSO Level 3.0 derived ratio of clear-sky AOD to above-cloud AOD to modify the aerosol amount over cloud over each grid cell in the MACR model. The Level 3.0 data have gaps. Again, the data gaps were filled using a linear interpolation, then the data was converted into the T42 grids, and the climatological seasonal cycle was obtained before use in the MACR model.

For coarse-mode aerosols, we apply the same profiles given a lack of observations. Because coarse-mode aerosols are not very absorbing, the effect of the vertical profile is very small (see Choi and Chung, 2014).

3 Radiation model

We use the MACR model as in Choi and Chung (2014), except that we improved the low cloud height in the model using the CALIPSO Level 2.0 data. As in Choi and Chung (2014), the height of low cloud bottom is set to 750 m above the ground. The low cloud top height is set to 1250 m, when the maximum low cloud height over a $5^\circ \times 2^\circ$ grid (and during a whole month) from CALIPSO data is 750 to 1750 m. When the CALIPSO maximum low cloud height exceeds 1750 m, the low cloud top height in the model is set to 1750 m above the ground.

This model was built upon the so-called Monte Carlo Independent Column Approximation (McICA) approach (Pincus et al., 2003); it uses a set of satellite observations to describe multilayer cloud, surface albedo and stratospheric column ozone, and it uses ERA-Interim Reanalyses (Dee et al., 2011) to describe the precipitable water. An earlier version has undergone comprehensive validation of the simulated fluxes at the TOA and at the surface over 100 land and island stations (agreement with observations is within a few Watts per square meter (Kim and Ramanathan, 2008). Only shortwave radiation is considered here.

4 Aerosol direct radiative effect

We first address the direct aerosol radiative effect (forcing due to natural and anthropogenic aerosols). We incorporated the integrated global aerosol data (as explained in Sect. 2) into the MACR model. Figure 1b shows the direct aerosol radiative effect as estimated by the MACR model. The direct aerosol radiative effect in Fig. 1b also incorporates the possibility that aerosol amount over cloud may differ from that at the same height in clear skies in the same region. The

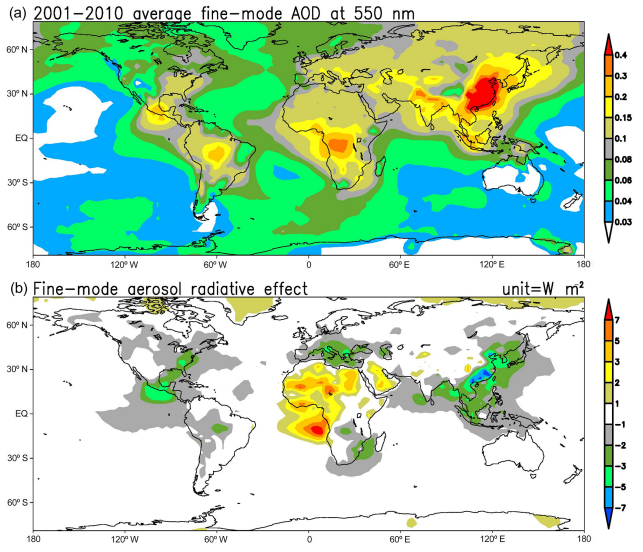

Figure 3. **(a)** The 2001–2010 mean 550 nm fine-mode AOD (fAOD) obtained by integrating MODIS, MISR and AERONET data. **(b)** The 2001–2010 mean direct fine-mode aerosol radiative effect at TOA in units of Watts per square meter; this estimate includes natural fine-mode particles.

CALIOP lidar is able to retrieve the aerosol amount over cloud as well as in clear skies, and so we used this lidar data to constrain the aerosol amount over cloud (as explained in Sect. 2.4) in computing the direct aerosol radiative effect. This procedure could be important since radiation modeling studies showed that the sensitivity of aerosol forcing to the aerosol vertical profile arises mainly as a consequence of the location of absorbing particles relative to cloud (Choi and Chung, 2014). On the other hand, cloud is brighter than most surfaces during daytime, and this could create a low bias in aerosol amount over cloud, as retrieved by the CALIOP lidar (Chepfer et al., 2013; Hunt et al., 2009; Kacenelenbogen et al., 2014; Vaughan et al., 2009). To be certain, we recomputed the aerosol radiative effect assuming equal amounts between clear skies and over cloud and found that the radiative effect only increases by 0.03 W m^{-2} on global average.

Next, we estimate the fine-mode aerosol radiative effect. Since the FMF of aerosols over land is difficult to accurately retrieve from satellites, past semiempirical estimates (Bellouin et al., 2008; Myhre, 2009) only used the FMF of AOD from satellite observations over the ocean. In contrast, AERONET data provide relatively reliable FMF over both land and ocean (with the AERONET data being predominantly over land). Following the approach of Lee and Chung (2013), satellite data are nudged toward AERONET data to construct global FMF and thus fine-mode AOD (see Sect. 2.1 for details). Figure 3a shows this fine-mode AOD, which, as expected, is largest over industrial and biomass burning areas.

Figure 3b shows the estimated fine-mode direct radiative effect as the difference between the coarse-mode and total (coarse + fine modes) aerosol radiative effect. The fine-mode radiative effect is negative almost everywhere, except over the eastern equatorial Atlantic, the Sahara and the Arabian Desert. These areas of positive forcing result from highly absorbing particles above highly reflective surfaces or low cloud. The global average of the fine-mode direct radiative effect is estimated as -0.46 W m^{-2}. In this computation, aerosol simulation using GOCART was used to provide interpolation for aerosol optical characteristics, such as SSA. To quantify uncertainty in the model dependence, two sets of additional simulations were conducted, representing lower and upper limits of absorption efficiency (see Sect. 2.2 and Fig. 2). The fine-mode radiative effect is estimated to range between -0.54 and -0.39 W m^{-2}, corresponding to these two limits (Table 1). Aerosol simulations yielding the fine-mode radiative effect outside of the -0.54 to -0.39 W m^{-2} range can be considered as inconsistent with observational constraints.

5 Fine-mode fraction (FMF) of sea salt and dust AODs

The fine-mode direct radiative effect estimate, as shown in Fig. 3b, includes the contribution from natural fine-mode sea salt and dust aerosols. To subtract this contribution from the fine-mode direct radiative effect estimate, we address the FMF of sea salt and dust AODs here. Instead of using simulated fine-mode sea salt and dust AOD (and thus being 100 % subject to model uncertainties), we use observed coarse-mode AOD $\times \frac{\text{SD\_FMF}}{1-\text{SD\_FMF}}$, where SD_FMF refers to the simulated FMF of sea salt + dust AOD. An underlying assumption therein is that coarse-mode AOD results only from sea salt and dust aerosols. We obtain the observed coarse-mode AOD by subtracting fine-mode AOD from total AOD, where the fine-mode and total AODs were obtained by integrating AERONET, MODIS and MISR data (see Sect. 2.1). On rare occasions, $\frac{\text{SD\_FMF}}{1-\text{SD\_FMF}}$ becomes unrealistically large. To prevent this, we limit fine-mode sea salt and dust AOD to being < 99 % of total fine-mode AOD.

For simulated FMF, we used AOD (at 550 nm) simulations from GOCART, the Spectral Radiation-Transport Model for Aerosol Species (SPRINTARS), the Tracer Model 5 (TM5) and ModelE2-TOMAS (ModelE2-TwO-Moment Aerosol Sectional microphysics module; ModelE2 used as short form here). The SPRINTARS output is from the AeroCom (Aerosol Comparisons between Observations and Models) Phase II (Schulz et al., 2009) hindcast experiments, and the TM5 outputs are from the AeroCom Phase III. The ModelE2-TOMAS simulation was performed using the TOMAS microphysics module incorporated into the state-of-the-art general circulation model GISS ModelE2 (Lee et al., 2015). The TOMAS module represents aerosol size distribution in many size categories or "bins" covering 10 nm to 10 µm. We used

a Fast-TOMAS module (Lee and Adams, 2012) with a 15-bin version here, since Fast TOMAS reduces the computational burden by 2–3 times while preserving the capability of computing fine-mode fraction well compared to the original TOMAS model with 30 bins. The fine-mode fraction of dust and sea salt aerosols from ModelE2-TOMAS was calculated by converting the mass output to AODs and then applying the spectral deconvolution algorithm (SDA) used in AERONET retrievals (O'Neill et al., 2003) to the AODs in order to create FMF consistent with AERONET FMF. A Mie-scattering code was used to compute size-resolved AOD at 380, 440, 500, 675 and 870 nm. Refractive indices for dust and sea salt are taken from Optical Properties of Aerosol and Clouds (OPAC) dataset (Hess et al., 1998). For other models, we calculated FMF using AODs from fine-mode aerosols and coarse-mode aerosols.

The ModelE2-TOMAS simulation was nudged with wind from MERRA (Modern Era Retrospective-analysis for Research and Applications) reanalysis from 2003 to 2005 after 3 years of spin-up. The simulation period for ModelE2-TOMAS is 2003–2005 and that for TM5, SPRINTARS and GOCART are 2001–2010, 2001–2008 and 2000–2007, respectively. Climatological AODs for each of four models were obtained by computing the average over the aforementioned simulation period for each calendar month.

Figure 4 is displayed to compare various simulated FMFs with the observed FMF. First, we assess which simulation performs the best in simulating dust FMF by looking at the simulated FMFs (including FMF of non-dust particles) over dust-dominated places where we use AERONET observations to validate the simulated FMFs. Dust-dominated AERONET sites in Fig. 4a were selected with the following criteria: 550 nm FMF < 0.3, AAE (absorption Ångström exponent) > 2.0 and 550 nm AAOD (absorption AOD) > 0.03. We again followed the approach by Lee and Chung (2013) in computing AERONET FMF, AAE and AAOD. Please note that in Fig. 4 we used climatological means for each calendar month; for FMF we again used mean AODs to compute the FMF instead of averaging FMFs. Figure 4b suggests that models tend to overestimate dust FMF, at least over dust-dominated places, as previously pointed out by Kok (2011).

Regarding sea salt FMF, we look at the simulated sea salt FMFs and observed total FMF over relatively pristine oceans (Fig. 4c). Organic and sulfate aerosols can be over remote oceans (Shank et al., 2012) in addition to fine-mode sea salt. Figure 4c shows large disagreements between sea salt FMF simulations, where one of the models (i.e., GOCART) clearly overestimates sea salt FMF given that the simulated sea salt FMF is near the total FMF from observations. In view of this, we scale down the simulated fine-mode dust FMF and mixed sea salt FMF simulations to calculate FMF of sea salt.

We scale down the simulated dust FMF and mixed sea salt FMF simulations by having multiple estimates (best estimate and sensitivity runs) to address the uncertainty in simulated FMF. The FMF of sea salt + dust AOD for our best estimate (i.e., baseline) is prepared using ModelE2 as follows. We scale up the coarse-mode dust AOD by 1.16 times and scale down the fine-mode dust AOD by 0.56 times so that ModelE2 would match AERONET FMF and AOD over dust-dominated sites. We scale down sea salt AOD (both fine and coarse modes) by 0.6 times so that the total AOD from ModelE2 matches AERONET data over sea-salt-dominated sites. We use ModelE2 for the best estimate since this model has an advanced size distribution description and uses the SDA to divide the AOD into fine-mode and coarse-mode components. For sensitivity run 1, we replace the ModelE2 dust

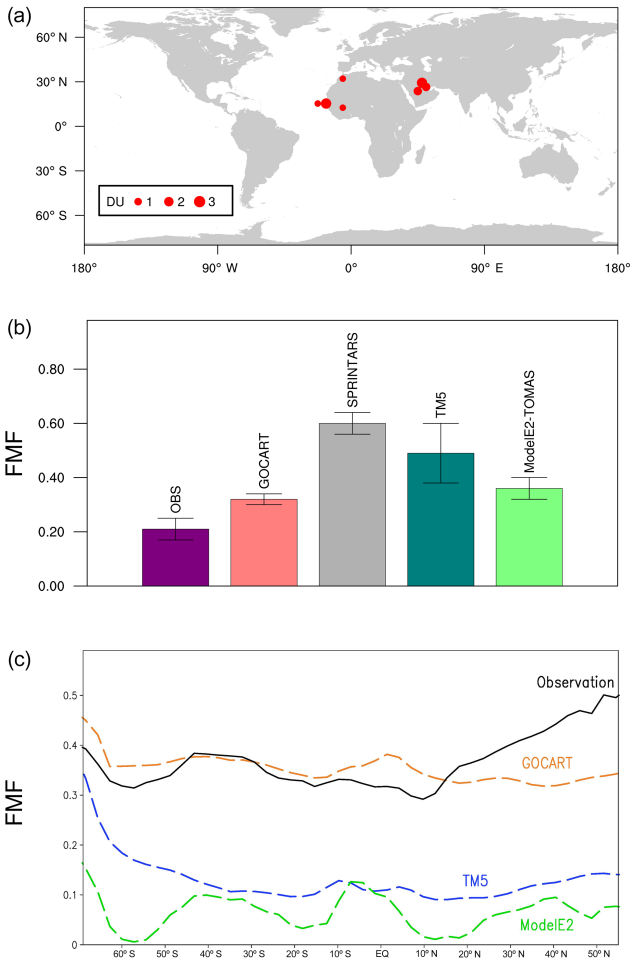

Figure 4. Comparison of simulated and observed fine-mode fraction (FMF) at 550 nm. **(a)** Chosen dust-dominated (DU: red dots) AERONET sites. The dot size is proportional to the number of AERONET data from decadal means (2001–2010) for each calendar month. **(b)** Simulated and observed FMF averaged over the chosen dust-dominated sites. FMF averages are made by the average AOD and fAOD. The uncertainty represents ±1.0 standard deviation resulting from variation over the sites. FMFs here include the contribution from non-dust particles. **(c)** Sea salt AOD FMF along the 180th meridian (180° longitude), using annual average AODs. For observation, total FMF (instead of sea salt AOD FMF) is displayed.

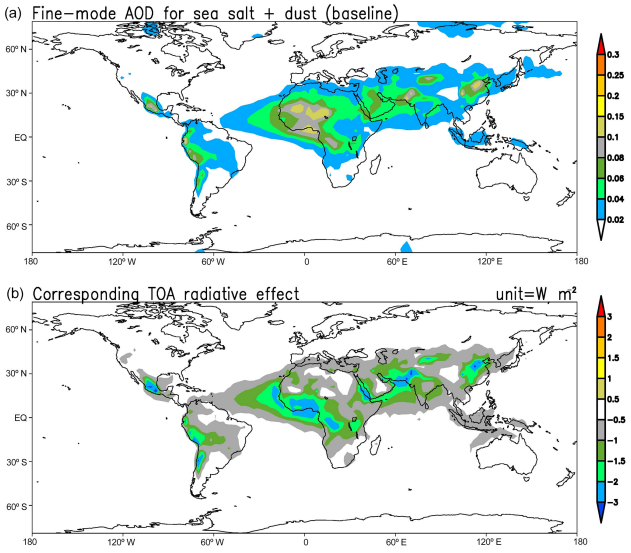

Figure 5. (a) The 2001–2010 mean fine-mode AOD at 550 nm for sea salt and dust, which is calculated as simulated ratio × observational large-mode AOD, where the simulated ratio refers to $\frac{\text{Model−mix fine-mode AOD for sea salt and dust}}{\text{Model−mix large-mode AOD for sea salt and dust}}$. The observational large-mode AOD is computed by integrating AERONET, MODIS and MISR data. Model mix is an optimal mixture of GOCART, TM5 and ModelE2-TOMAS AOD simulations. **(b)** Aerosol direct radiative effect due to the sea salt and dust fine-mode aerosols.

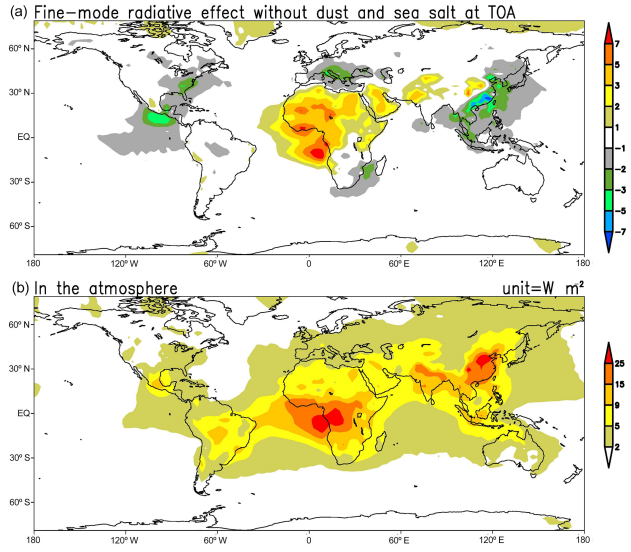

Figure 6. Direct fine-mode aerosol radiative effect without dust and sea salt in units of Watts per square meter (baseline); 2001–2010 mean values.

AOD by the GOCART dust AOD, where the coarse-mode dust AOD is scaled up by 1.3 times and the fine-mode dust AOD is scaled down by 0.74 times. For sensitivity run 2, we use the baseline setup except that for sea salt AOD we equally mix the outputs from GOCART, TM5 and ModelE2.

Scaling the simulated dust FMF to match AERONET FMF over dust-dominated sites may still have an overestimation or underestimation of dust FMF outside of dust-dominated regions. Moreover, dust-dominated regions have non-dust particles, and thus the scaled dust FMF may still underestimate or overestimate dust FMF even over dust-dominated regions. This is why we conduct sensitivity runs even after the scaling of the simulated dust FMF.

6 Implications for global direct aerosol radiative forcing

We estimate the direct radiative effect due to fine-mode sea salt and dust aerosols to be -0.35 (-0.44 to -0.26) W m^{-2} (Table 1). The spatial pattern is shown in Fig. 5. As mentioned in Sect. 5, our estimate of fine-mode sea salt and dust aerosols may be too large or too small over some areas. Possible overestimation or underestimation is likely reduced in the global average, and so we focus on global averages as shown in Table 1. The global direct radiative effect of -0.35 W m^{-2} is quite large. In those studies where fine-mode sea salt and dust aerosols were assumed to be negligible, the aerosol direct forcing estimates would have been that much more negative than in reality.

When we remove the contribution of fine-mode sea salt and dust aerosols from the fine-mode radiative effect, we end up with the aerosol radiative effect due to total (i.e., anthropogenic + natural) carbonaceous, sulfate and nitrate aerosols. As Fig. 6a shows, this radiative effect is large and positive over Africa and the downstream areas where biomass burning is the major source. The forcing is also conspicuously positive over the Sahara (Fig. 6a), partly because biomass burning aerosols in the Sahel are advected northwards in boreal winter (Haywood et al., 2008) and bright desert surfaces turn the forcing positive. Figure 6b shows that these advected aerosols have a relatively small forcing in the atmosphere due to smaller aerosol amounts. Outside of Africa and the downstream areas, the forcing is a mixture of positive and negative values, and negative values slightly outweigh positive values. The global average (including Africa) of the TOA forcing (as shown in Fig. 6a) is -0.11 W m^{-2} with an uncertainty range of -0.28 to $+0.05$ W m^{-2}, which results from $-0.54 + 0.26$ to $-0.39 + 0.44$ W m^{-2}.

The consensus of global aerosol direct radiative forcing as shown in the 5th IPCC report is -0.35 W m^{-2} (Myhre et al., 2013a), and this includes a dust forcing of -0.10 W m^{-2}. Thus, the IPCC estimate is that anthropogenic carbonaceous, sulfate and nitrate aerosols result in a radiative forcing of -0.25 W m^{-2}, while our observational estimate of total (anthropogenic + natural) carbonaceous, sulfate and nitrate aerosol forcing is -0.11 W m^{-2}. The anthropogenic fraction (or preindustrial fraction) of carbonaceous, sulfate and nitrate aerosols is uncertain. Black carbon, the only

warming aerosol species in carbonaceous aerosol (black carbon + organic aerosol), sulfate and nitrate aerosol is known to be more anthropogenic than organic aerosols are (Bond et al., 2011). If the anthropogenic fraction of black carbon is similar to that of nitrate and sulfate aerosol, the aerosol direct radiative forcing becomes $> -0.11\,\mathrm{W\,m^{-2}}$ in our observational estimation, which means that aerosol direct forcing is less negative than the consensus expressed in the 5th IPCC report.

Our observational approach makes the results subject to observation errors. AERONET SSA, in particular, is subject to potentially significant uncertainties due to various assumptions used in the retrieval algorithms. Thus, the uncertainty in our estimates of fine-mode forcing may be larger than -0.54 to $-0.39\,\mathrm{W\,m^{-2}}$. However, studies (Eck et al., 2010; Leahy et al., 2007) showed that AERONET SSA is higher or lower than in situ measurements depending on location, season, in situ measurement device, etc. Furthermore, in situ measurements are also subject to uncertainties, and so the difference between the AERONET SSA and in situ measured SSA is not necessarily due only to the AERONET data error. Overall, we believe that AERONET observations likely have smaller biases and provide more credible results than aerosol simulations. At the very least, our observational approach offers a more independent estimate than pure aerosol simulations.

Acknowledgements. The authors are thankful to P. Adams of Carnegie Mellon University and N. T. O'Neill at the Canadian Network for the Detection of Atmospheric Change for valuable input. This study was funded by the National Science Foundation (AGS-1455759). Jung-Eun Chu's participation was supported by an NRF (National Research Foundation of Korea) grant (NRF-2013-Fostering Core Leaders of the Future Basic Science Program).

Edited by: A. Laaksonen

References

Bellouin, N., Jones, A., Haywood, J., and Christopher, S. A.: Updated estimate of aerosol direct radiative forcing from satellite observations and comparison against the Hadley Centre climate model, J. Geophys. Res.-Atmos., 113, D10205, doi:10.1029/2007JD009385, 2008.

Bond, T. C., Streets, D. G., Yarber, K. F., Nelson, S. M., Woo, J.-H., and Klimont, Z.: A technology-based global inventory of black and organic carbon emissions from combustion, J. Geophys. Res., 109, D14203, doi:10.1029/2003JD003697, 2004.

Bond, T. C., Zarzycki, C., Flanner, M. G., and Koch, D. M.: Quantifying immediate radiative forcing by black carbon and organic matter with the Specific Forcing Pulse, Atmos. Chem. Phys., 11, 1505–1525, doi:10.5194/acp-11-1505-2011, 2011.

Chepfer, A., Cesana, G., Winker, M. A., Getzewich, B., Vaughan, K. A., and Liu, Z.: Comparison of two different cloud climatologies derived from CALIOP-attenuated backscattered measurements (Level 1): The CALIPSO-ST and the CALIPSO-GOCCP, J. Atmos. Ocean. Tech., 30, 725–744, 2013.

Chin, M., Ginoux, P., Kinne, S., Torres, O., Holben, B. N., Duncan, B. N., Martin, R. V., Logan, J. A., Higurashi, A., and Nakajima, T.: Tropospheric aerosol optical thickness from the GOCART model and comparisons with satellite and sun photometer measurements, J. Atmos. Sci., 59, 461–483, 2002.

Choi, J.-O. and Chung, C. E.: Sensitivity of aerosol direct radiative forcing to aerosol vertical profile, Tellus B, 66, 24376, doi:10.3402/tellusb.v66.24376, 2014.

Chung, C. E.: Aerosol Direct Radiative Forcing: A Review, INTECH, doi:10.5772/50248, 2012.

Chung, C. E., Ramanathan, V., and Decremer, D.: Observationally constrained estimates of carbonaceous aerosol radiative forcing, P. Natl. Acad. Sci., 109, 11624–11629, 2012.

Chung, C. E., Ramanathan, V., Kim, D., and Podgorny, I. A.: Global anthropogenic aerosol direct forcing derived from satellite and ground-based observations, J. Geophys. Res., 110, D24207, doi:10.1029/2005JD006356, 2005.

Dee, D. P., Uppala, S. M., Simmons, A. J., Berrisford, P., Poli, P., Kobayashi, S., Andrae, U., Balmaseda, M. A., Balsamo, G., Bauer, P., Bechtold, P., Beljaars, A. C. M., van de Berg, L., Bidlot, J., Bormann, N., Delsol, C., Dragani, R., Fuentes, M., Geer, A. J., Haimberger, L., Healy, S. B., Hersbach, H., Hólm, E. V., Isaksen, L., Kållberg, P., Köhler, M., Matricardi, M., McNally, A. P., Monge-Sanz, B. M., Morcrette, J. J., Park, B. K., Peubey, C., de Rosnay, P., Tavolato, C., Thépaut, J. N., and Vitart, F.: The ERA-Interim reanalysis: configuration and performance of the data assimilation system, Q. J. Roy. Meteor. Soc., 137, 553–597, 2011.

Eck, T. F., Holben, B. N., Sinyuk, A., Pinker, R. T., Goloub, P., Chen, H., Chatenet, B., Li, Z., Singh, R. P., Tripathi, S. N., Reid, J. S., Giles, D. M., Dubovik, O., O'Neill, N. T., Smirnov, A., Wang, P., and Xia, X.: Climatological aspects of the optical properties of fine/coarse mode aerosol mixtures, J. Geophys. Res., 115, D19205, doi:10.1029/2010JD014002, 2010.

Haywood, J. M., Pelon, J., Formenti, P., Bharmal, N., Brooks, M., Capes, G., Chazette, P., Chou, C., Christopher, S., Coe, H., Cuesta, J., Derimian, Y., Desboeufs, K., Greed, G., Harrison, M., Heese, B., Highwood, E. J., Johnson, B., Mallet, M., Marticorena, B., Marsham, J., Milton, S., Myhre, G., Osborne, S. R., Parker, D. J., Rajot, J.-L., Schulz, M., Slingo, A., Tanré, D., and Tulet, P.: Overview of the Dust and Biomass-burning Experiment and African Monsoon Multidisciplinary Analysis Special Observing Period-0, J. Geophys. Res.-Atmos., 113, D00C17, doi:10.1029/2008JD010077, 2008.

Hess, M., Koepke, P., and Schult, I.: Optical Properties of Aerosols and Clouds: The Software Package OPAC, B. Am. Meteorol. Soc., 79, 831–844, 1998.

Holben, B. N., Eck, T. F., Slutsker, I., Tanre, D., Buis, J. P., Setxer, A., Vermote, E., Reagan, J. A., Kaufman, Y. J., Nakajima, T., Lavenu, F., Jankowiak, I., and Smirnov, A.: AERONET – A federated instrument network and data archive for aerosol characterization, Remote Sens. Environ., 66, 1–16, 1998.

Hunt, W. H., Winker, M. A., Vaughan, K. A., Powell, K. A., Lucker, P. L., and Weimer, C.: CALIPSO Lidar description and performance assessment, J. Atmos. Ocean. Tech., 26, 1214–1228, 2009.

Kacenelenbogen, M., Redemann, J., Vaughan, M. A., Omar, A. H., Russell, P. B., Burton, S., Rogers, R. R., Ferrare, R. A., and Hostetler, C. A.: An evaluation of CALIOP/CALIPSO's aerosol-above-cloud (AAC) detection and retrieval capability, J. Geophys. Res.-Atmos., 119, 230–244, 2014.

Kim, D. and Ramanathan, V.: Solar radiation budget and radiative forcing due to aerosols and clouds, J. Geophys. Res., 113, D02203, doi:10.1029/2007JD008434, 2008.

Kim, J., Jung, C. H., Choi, B. C., Oh, S. N., Brechtel, F. J., Yoon, S. C., and Kim, S. W.: Number size distribution of atmospheric aerosols during ACE-Asia dust and precipitation events, Atmos. Environ., 41, 4841–4855, 2007.

Kok, J. F.: A scaling theory for the size distribution of emitted dust aerosols suggests climate models underestimate the size of the global dust cycle, P. Natl. Acad. Sci., 108, 1016–1021, 2011.

Leahy, L. V., Anderson, T. L., Eck, T. F., and Bergstrom, R. W.: A synthesis of single scattering albedo of biomass burning aerosol over southern Africa during SAFARI 2000, Geophys. Res. Lett., 34, L12814, doi:10.1029/2007GL029697, 2007.

Lee, K. and Chung, C. E.: Observationally-constrained estimates of global fine-mode AOD, Atmos. Chem. Phys., 13, 2907–2921, doi:10.5194/acp-13-2907-2013, 2013.

Lee, Y. H. and Adams, P. J.: A Fast and Efficient Version of the TwO-Moment Aerosol Sectional (TOMAS) Global Aerosol Microphysics Model, Aerosol Sci. Tech., 46, 678–689, 2012.

Lee, Y. H., Adams, P. J., and Shindell, D. T.: Evaluation of the global aerosol microphysical ModelE2-TOMAS model against satellite and ground-based observations, Geosci. Model Dev., 8, 631–667, doi:10.5194/gmd-8-631-2015, 2015.

Liu, Z., Vaughan, M., Winker, D., Kittaka, C., Getzewich, B., Kuehn, R., Omar, A., Powell, K., Trepte, C., and Hostetler, C.: The CALIPSO Lidar Cloud and Aerosol Discrimination: Version 2 Algorithm and Initial Assessment of Performance, J. Atmos. Ocean. Tech., 26, 1198–1213, 2009.

Ma, X., Yu, F., and Luo, G.: Aerosol direct radiative forcing based on GEOS-Chem-APM and uncertainties, Atmos. Chem. Phys., 12, 5563–5581, doi:10.5194/acp-12-5563-2012, 2012.

Magi, B. I.: Chemical apportionment of southern African aerosol mass and optical depth, Atmos. Chem. Phys., 9, 7643–7655, doi:10.5194/acp-9-7643-2009, 2009.

Magi, B. I.: Corrigendum to "Chemical apportionment of southern African aerosol mass and optical depth" published in Atmos. Chem. Phys., 9, 7643–7655, 2009, Atmos. Chem. Phys., 11, 4777–4778, doi:10.5194/acp-11-4777-2011, 2011.

Myhre, G., Shindell, D., Bréon, F.-M., Collins, W., Fuglestvedt, J., Huang, J., Koch, D., Lamarque, J.-F., Lee, D., Mendoza, B., Nakajima, T., Robock, A., Stephens, G., Takemura, T., Zhang, H., Aamaas, B., Boucher, O., Dalsøren, S. D., Daniel, J. S., Forster, P., Granier, C., Haigh, J., Hodnebrog, Ø., Kaplan, J. O., Marston, G., Nielsen, C. J., O'Neill, B. C., Peters, G. P., Pongratz, J., Prather, M., Ramaswamy, V., Roth, R., Rotstayn, L., Smith, S. J., Stevenson, D., Vernier, J.-P., Wild, O., and Young, P.: Anthropogenic and Natural Radiative Forcing, in: Climate Change 2013: The Physical Science Basis. Contribution of Working Group I to the Fifth Assessment Report of the Intergovernmental Panel on Climate Change, IPCC report, V, 2013a.

Myhre, G., Samset, B. H., Schulz, M., Balkanski, Y., Bauer, S., Berntsen, T. K., Bian, H., Bellouin, N., Chin, M., Diehl, T., Easter, R. C., Feichter, J., Ghan, S. J., Hauglustaine, D., Iversen, T., Kinne, S., Kirkevåg, A., Lamarque, J.-F., Lin, G., Liu, X., Lund, M. T., Luo, G., Ma, X., van Noije, T., Penner, J. E., Rasch, P. J., Ruiz, A., Seland, Ø., Skeie, R. B., Stier, P., Takemura, T., Tsigaridis, K., Wang, P., Wang, Z., Xu, L., Yu, H., Yu, F., Yoon, J.-H., Zhang, K., Zhang, H., and Zhou, C.: Radiative forcing of the direct aerosol effect from AeroCom Phase II simulations, Atmos. Chem. Phys., 13, 1853–1877, doi:10.5194/acp-13-1853-2013, 2013b.

Myhre, G.: Consistency between satellite-derived and modeled estimates of the direct aerosol effect, Science, 325, 187–190, 2009.

O'Neill, J. T., Eck, T. F., Smirnov, A., Holben, B. N., and Thulasiraman, S.: Spectral discrimination of coarse and fine mode optical depth, J. Geophys. Res., 108, 4559, doi:10.1029/2002JD002975, 2003.

Pincus, R., Barker, H. W., and Morcrette, J.-J.: A fast, flexible, approximate technique for computing radiative transfer in inhomogeneous cloud fields, J. Geophys. Res., 108, 4376, doi:10.1029/2002JD003322, 2003.

Schulz, M., Chin, M., and Kinne, S.: The aerosol model comparison project, AeroCom, phase II: clearing up diversity, IGAC Newsletter, IGAC Core Project Office, Research Center for Environmental Change, Taipei, Taiwan, 2009.

Shank, L. M., Howell, S., Clarke, A. D., Freitag, S., Brekhovskikh, V., Kapustin, V., McNaughton, C., Campos, T., and Wood, R.: Organic matter and non-refractory aerosol over the remote Southeast Pacific: oceanic and combustion sources, Atmos. Chem. Phys., 12, 557–576, doi:10.5194/acp-12-557-2012, 2012.

Su, W., Loeb, N. G., Schuster, G. L., Chin, M., and Rose, F. G.: Global all-sky shortwave direct radiative forcing of anthropogenic aerosols from combined satellite observations and GOCART simulations, J. Geophys. Res.-Atmos., 118, 655–669, 2013.

Vaughan, M. A., Powell, K. A., Winker, D. M., Hostetler, C. A., Kuehn, R. E., Hunt, W. H., Getzewich, B. J., Young, S. A., Liu, Z., and McGill, M. J.: Fully automated detection of cloud and aerosol layers in the calipso lidar measurements, J. Atmos. Ocean. Tech., 26, 2034–2050, 2009.

Viskari, T., Asmi, E., Virkkula, A., Kolmonen, P., Petäjä, T., and Järvinen, H.: Estimation of aerosol particle number distribution with Kalman Filtering – Part 2: Simultaneous use of DMPS, APS and nephelometer measurements, Atmos. Chem. Phys., 12, 11781–11793, doi:10.5194/acp-12-11781-2012, 2012.

Winker, D. M., Tackett, J. L., Getzewich, B. J., Liu, Z., Vaughan, M. A., and Rogers, R. R.: The global 3-D distribution of tropospheric aerosols as characterized by CALIOP, Atmos. Chem. Phys., 13, 3345–3361, doi:10.5194/acp-13-3345-2013, 2013.